CHALMERS
UNIVERSITY OF TECHNOLOGY

Microwave Imaging With a Reduced Number of Transmission Channels in a Semi-Circular Antenna Array

Citation for the original published paper (version of record):
Guerrero Orozco, L., Peterson, L., Fhager, A. (2025). Microwave Imaging With a Reduced Number of Transmission Channels in a Semi-Circular Antenna
Array. IEEE Journal of Electromagnetics, RF and Microwaves in Medicine and Biology, 9(4): 500-507. http://dx.doi.org/10.1109/JERM.2025.3596876

Microwave Imaging With a Reduced Number of Transmission Channels in a Semi-Circular Antenna Array

Laura Guerrero Orozco, Lars Peterson, and Andreas Fhager, *Member, IEEE*

***Abstract*—Muscle injuries, particularly in the muscles composing the hamstring, pose significant challenges in sports medicine. Our aim is to use microwaves for the diagnosis of such injuries with a compact and low-cost system. A primary challenge with compact systems is the measurement time, caused by the time needed to switch between transmission channels. In this study, we explore the potential for reducing the number of transmission channels in a semi-circular antenna array and its impact on reconstruction accuracy. We hypothesized that antennas closer to each other are more important for accurate reconstruction due to their higher coherency, signal strength and lower noise levels compared to distant antennas. Thus, the farthest antennas may be excluded from measurements and reconstructions. Using both simulations and measurements, we systematically decreased the number of transmission channels to observe the effects on the reconstructed image. Our findings demonstrate that it is feasible to reduce the number of transmission channels by omitting the farthest antennas from 56 down to 36 channels while limiting the reduction in Signal to clutter ratio (SCR) to less than 12%.**

***Index Terms*—Microwave imaging, medical diagnosis, transmission channels, muscle rupture, image reconstruction, prototype.**

I. Introduction

MUSCLE injuries pose a significant challenge in sports medicine, often keeping athletes sidelined for long recovery periods [1]. In our previous work [2], [3], we introduced a semi-circular microwave system to image the dielectric contrast between blood and surrounding muscle and proposed an antenna design that attenuates unwanted signals, improving image reconstruction accuracy and stability across repeated tests.

A semi-circular antenna array is appealing as it simplifies the design and operation of a muscle rupture detector. However, most 2D microwave imaging studies use full-circle arrays. Therefore, it is interesting to investigate the differences in image reconstruction accuracy between these two types of arrays. One of the goals of this paper is to study how a reduced antenna array affects the image reconstruction accuracy.

Given the need for a compact, low-cost system that can be deployed on-site by sports medicine teams or in primary care units, we investigated the measurement quality of software-defined radio (SDR) hardware [4]. Encouraged by these results, we aim to replace the costly multi-port vector network analyzer (VNA) with an SDR to reduce size and cost. However, SDRs and other compact instruments (e.g., 2-port VNAs) require sequential transmission channel switching, which increases measurement time. Thus, it is advantageous to minimize the number of antennas and transmission channels as much as possible while maintaining acceptable imaging accuracy. Multi-static systems aim to maximize the number of active antennas, but the optimal number of antennas and transmission channels depends on the specific application and imaging approach [5], [6], [7], [8], [9], [10], [11], [12], [13]. In a fully multi-static system, every antenna both transmits and receives, so the number of transmission channels grows exponentially, increasing acquisition time, computational complexity, and cost [7]. Instead of focusing on the number of antennas, this work explores reducing the number of transmission channels.

Other research efforts have focused on evaluating reconstructions using different combinations of transmission channels. For example, various weighted delay-and-sum beamformers have been proposed [10], [14], [15], [16], assigning greater weight to closely spaced antennas, which tend to exhibit higher coherency than those farther apart. This study tests the hypothesis that antennas spaced farther apart provide less useful information due to lower channel coherence, increased signal attenuation, and and elevated noise levels. If correct, these channels could be omitted or not measured to reduce the number of measurements without noticeably reducing image reconstruction accuracy. To evaluate this, image reconstructions were performed with a gradually reduced number of transmission channels, and the resulting images were quantitatively assessed for position, shape, and contrast of the bleedings. Comparisons were also made against a fully-circular array. The rest of this paper is organized as follows. Section II outlines the proposed channel-reduction method, the measurement and simulation setups, and the image evaluation metrics. Section III presents the reconstruction results for the circular and semi-circular arrays and evaluates image quality as the number of transmission channels is reduced. Finally, Section IV discusses the findings, and Section V provides the conclusions.

Received 12 December 2024; revised 1 April 2025 and 23 June 2025; accepted 29 July 2025. Date of publication 19 August 2025; date of current version 22 November 2025. This work was supported in part by Strengthened Collaboration Environments through MedTechWest under Project 20201637 funded by European Regional Development Fund through the Swedish Agency for Economic and Regional Growth (Tillväxtverket) and in part by the internal funds at Chalmers University of Technology. *(Corresponding author: Andreas Fhager.)*

Laura Guerrero Orozco and Andreas Fhager are with the Department of Electrical Engineering, Chalmers University of Technology, 41296 Gothenburg, Sweden (e-mail: andreas.fhager@chalmers.se).

Lars Peterson is with the Sahlgrenska Academy, University of Gothenburg, 40530 Gothenburg, Sweden (e-mail: peterson.lars@telia.com).

Digital Object Identifier 10.1109/JERM.2025.3596876

II. Methods

The image reconstruction quality as a function of the number of transmission channels was investigated using both simulated and measured data. The simulations were made to allow comparison with various experimental scenarios, similar to the descriptions in [2], [3]. Both simulations and measurements involved only two tissue types: muscle, representing the leg's hamstring area, and blood, simulating bleeding accompanying a muscle rupture.

The Delay Multiply And Sum (DMAS) algorithm [17] was used for image reconstructions and it was operated in a multistatic configuration. Image quality was measured with metrics to quantify the accuracy of localization, shape and contrast.

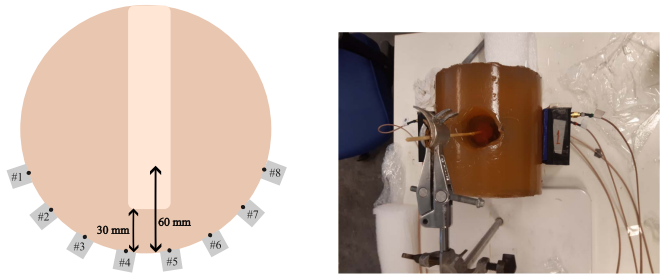

(a) Illustration of measurement setup including the bottom positions of two blood phantoms used in measurements.

(b) Top view of muscle phantom. The wooden stick holding the blood phantom is also seen.

Fig. 1. Illustration and picture of the experimental setup.

A. Simulations

Simulations were performed similar to the description in [2], which however only dealt with homogeneous muscle tissue. In this study, blood phantoms were added to evaluate reconstruction accuracy. Additionally, simulations with a circular antenna array were included to compare results with those from the semi-circular array.

Two sets of simulations were conducted:

- *Semi-circular Array (8 Antennas):* The first set involved arranging the antennas in a semi-circular antenna array comprising eight transmitter/receiver antennas spaced at angular intervals of 20°. This arrangement focuses the coverage to the lower part of the muscle, where bleeds are anticipated. A similar strategy of placing the antennas towards the bottom of a hemisphere was used by Klemm et al. [9], [18] for breast imaging. Given the size of the antennas, 8 is the maximum number of antennas that in an array that can fit a realistically sized leg. Electromagnetic performance of the antenna array, such as S-parameters, antenna coupling, and near-field radiation patterns have been thoroughly investigated in our previous work [2].
- *Circular Array (16 Antennas):* The second set comprised a circular array consisting of 16 antennas. Here, the antennas were divided into two subgroups of 8 antennas each, spaced at angular intervals of 20°. One subgroup was positioned at the top and the other at the bottom of the circular array.

The system was modeled with monopole antennas embedded in lossy gel, matching the dimensions used in experiments. The gel's dielectric properties were nearly constant across the relevant frequency range and thus approximated as constants to simplify simulations. The plastic cups holding the gel in experiments were excluded. The muscle phantom was modeled as a cylinder (160 mm diameter, 80 mm length), and blood phantoms matched the sizes and positions used in measurements [2], [3], shown with red dotted circles in Fig. 2. Material properties were based on measured values: at 1 GHz, muscle permittivity $\varepsilon = 52.58$ and conductivity $\sigma = 1.05$ S/m; blood permittivity $\varepsilon = 60.7$ and conductivity $\sigma = 1.5$ S/m. Simulations were run in CST Studio Suite 2020.07 over 0.5–3 GHz without added noise.

Before DMAS image reconstruction, early-time signal content was removed by subtracting lesion-free reference data (muscle only) from object data (muscle and blood), following our previous studies. Two simulation types were conducted: reference (muscle only) and object (with blood phantom), consistent with the experimental setup.

B. Measurement

Measurements were performed using the same system as in [2], [3], with both a homogeneous muscle phantom (reference) and blood phantoms present (object). The cylindrical muscle phantom measured 160 mm in diameter and had a 30 mm deep hole filled with liquid muscle phantom of matching properties to allow easy insertion of the blood phantoms, as shown in Fig. 1(a).

Fig. 1(b) shows the system setup, including the muscle phantom and the aperture for the blood phantom, which was mounted on a wooden stick for easy placement and removal. Measurements were taken with and without the blood phantom.

A 16-channel vector network analyzer (Rohde & Schwarz ZNBT8) measured signals over 0.5–2.0 GHz. The antennas were connected via flexible coaxial cables and SMA connectors.

C. Metrics for Image Evaluation

The accuracy of the reconstructed images was evaluated using metrics measuring the localization of the blood phantom and the contrast between blood response and clutter. These metrics include localization-based, shape, and artefact-to-object measures. The localization-based metric (Δr) is defined as the Euclidean distance between the true and reconstructed bleeding positions, with the latter identified as the pixel of maximum intensity, calculated as:

$$\Delta r = |P_{\text{max}} - P_{\text{blood}}|, \tag{1}$$

where P_{max} is the position of maximum intensity in the reconstructed bleeding, and P_{blood} is the known center of the blood phantom. For a true position of $(80, 30)$ mm and a reconstructed position of $(82, 32)$ mm, the localization error is about 2.82 mm.

For shape and contrast metrics, the target region Ω_b was defined as the area inside the full-width at half maximum (FWHM) boundary of the bleeding peak, where

$$I_r \geq \frac{1}{2} I_r max,$$

with I_r being individual pixel values and $I_r max$ the maximum pixel value of the reconstructed bleeding image. Pixels outside

Ω_b form the clutter region Ω_c. For reconstructions with the circular array, only the bottom half of the image region, $y \leq 80$ mm, was included to fairly compare with the semi-circular array.

The contrast metrics were defined as [19]:

- Signal to Clutter ratio (SCR),

$$SCR = 20 * \log_{10}\left(\frac{\langle I_r(\Omega_b)\rangle}{\langle I_r(\Omega_c)\rangle}\right) \tag{2}$$

- Contrast to noise ratio (CNR),

$$CNR = \frac{|\langle I_r(\Omega_b)\rangle - \langle I_r(\Omega_c)\rangle|}{\sqrt{\sigma^2_{\Omega_b} + \sigma^2_{\Omega_c}}} \tag{3}$$

Here, $\langle\cdot\rangle$ denotes the average and σ^2 the variance. Accurate reconstruction is indicated by low localization error (Δr) and high SCR and CNR. For example, a reconstructed bleeding region with average intensities of 0.73 inside and 0.02 outside yields an SCR of about 30 dB.

The shape of the reconstructed bleeding were analyzed on terms of its normalized height to width ratio (HWR), calculated as

$$HWR = \frac{height_{\Omega_b}/width_{\Omega_b}}{height_{blood}/width_{blood}}. \tag{4}$$

The height-to-width ratio (HWR) of the target Ω_b is divided by the known HWR of the blood phantom. An HWR of 1 indicates accurate shape reconstruction; deviations indicate distortion. For example, a reconstructed size of 30 mm by 20 mm versus an expected 20 mm by 20 mm gives an HWR of 1.33, showing elongation.

D. Image Reconstruction Accuracy Vs. Number of Transmission Channels

Our antenna array consisted of 8 antennas, resulting in up to $8 \times 8 = 64$ signal paths. First, the reflection measurements were excluded, leaving at most 56 transmission channels. Images were reconstructed while gradually excluding an increasing number of transmission channels. A first reduction was made by excluding the farthest antenna pairs, i.e. S_{18} and S_{81}, leaving 54 of the 56 channels. The next reconstruction was made with 50 combinations, excluding the additional channels $S_{17}, S_{71}, S_{28}, S_{82}$. In this way antenna pairs were excluded until only nearest neighbor antenna combinations remained, i.e. $S_{12}, S_{21}, S_{23}, S_{32}, \ldots, S_{78}, S_{87}$, resulting in 14 signal path combinations.

III. Results

A. Comparison of Semi-Circular Vs. Circular Antenna Arrays

The difference in reconstruction accuracy between the fully-circular and semi-circular arrays was investigated using simulated data. Images were reconstructed using a semi-circular array of 8 antennas (56 transmission channels) and a circular array of 16 antennas (240 transmission channels), as shown in Fig. 2 and Fig. 3, respectively. Four different cases were examined, with the true shapes and locations of the blood phantoms indicated by red dashed lines. The figures also show the reconstructed bleedings, along with the FWHM regions outlined by a red dotted line and the position of the maximum intensity pixel marked by a magenta point.

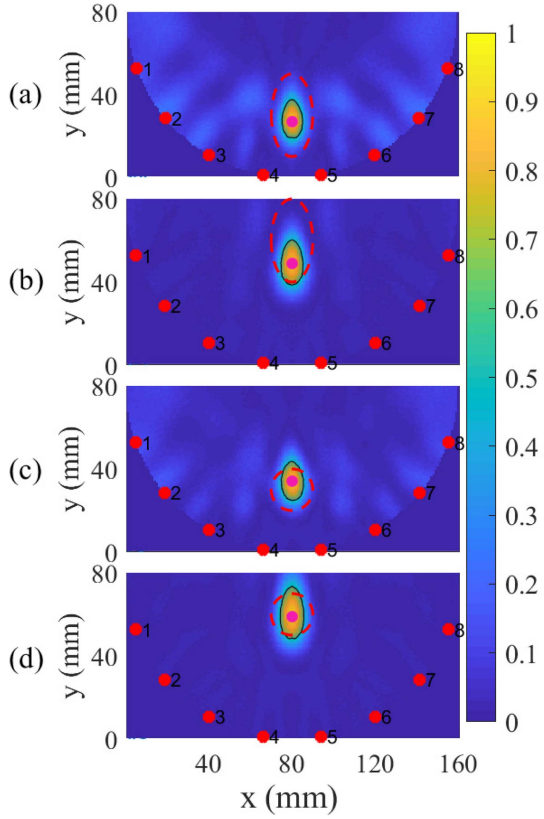

Fig. 2. Reconstructed images using 8 antennas (56 channels) for (a) Case 1, (b) Case 2, (c) Case 3, and (d) Case 4.

The positions of the reconstructed objects were evaluated using the localization error defined in (1), with results for the four cases shown in Fig. 4(a). In all cases, a single maximum intensity point was found within the expected blood phantom boundaries. In some reconstructions, this point closely matched the phantom's center, while in others it was nearer to the edges, resulting in higher localization errors, as seen in Case 2. For this case, the semi-circular array localized the target near the bottom of the image, whereas the circular array produced two target regions near the top and bottom. Thus, the shape of the target region depends on both the phantom's size and position.

The shape of the reconstructed objects was assessed using the HWR metric, with results in Fig. 4(b). For ellipsoidal phantoms (Cases 1 and 2), both arrays reconstructed FWHM areas accurately as ellipsoids, with HWR ratios close to 1. For circular phantoms (Cases 3 and 4), the circular array provided more accurate shape reconstructions than the semi-circular array. This suggests that the extra antennas in the full circular array contribute more to shape accuracy than to localization.

Image quality was further evaluated using contrast metrics, SCR and CNR, defined in (2) and (3), with results shown in Fig. 5. The SCR values were high (SCR $>$ 15 dB) for all cases

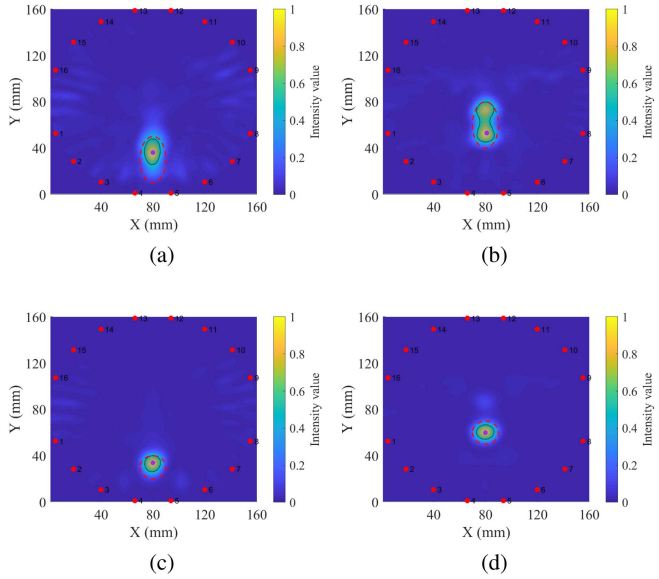

Fig. 3. Reconstructed images using 16 antennas (240 channels) for (a) Case 1, (b) Case 2, (c) Case 3, and (d) Case 4.

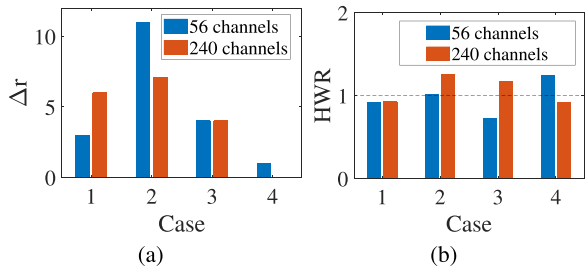

Fig. 4. (a) Δr and (b) HWR ratio for semi-circular and circular array obtained using 56 transmission channels and 240 transmission channels.

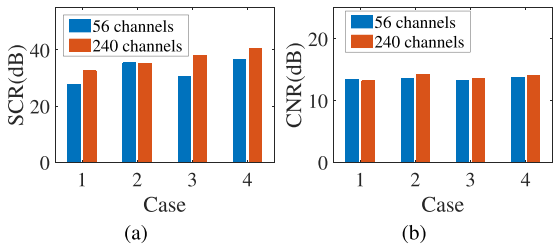

Fig. 5. (a) SCR and (b) CNR obtained using 56 transmission channels and 240 transmission channels.

and both array types, indicating that the reconstructed objects were clearly distinguishable from clutter. The circular array yielded higher SCR values, improving by 4–8 dB compared to the semi-circular array. In contrast, the CNR remained fairly consistent between the two arrays, suggesting that while the clutter magnitude stayed similar, the semi-circular array experienced more clutter overall. This result is consistent with expectations, as a greater number of antenna channels typically enhances clutter rejection [17].

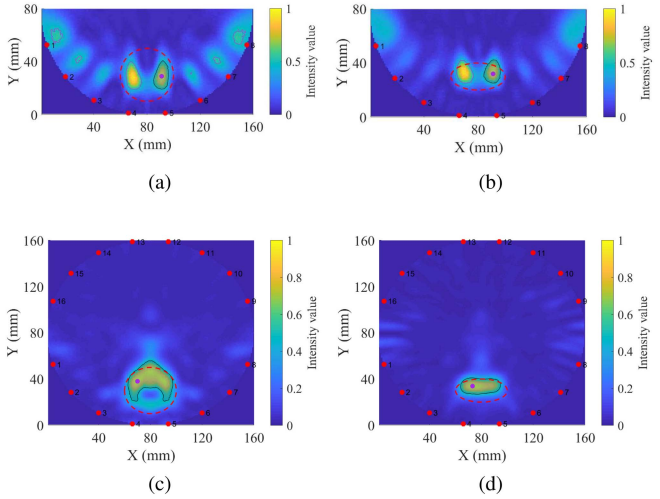

Fig. 6. Reconstructed images of larger bleedings. (a) Case 5 with 8 antennas (56 channels), (b) Case 6 with 8 antennas (56 channels), (c) Case 5 with 16 antennas (240 channels), and (d) Case 6 with 16 antennas (240 channels).

We examined reconstructions of larger, horizontally oriented elliptical bleedings (Cases 5 and 6, Fig. 6). While the reconstructed objects and peak intensities stayed within true boundaries, the targets often appeared split or hollow—a known issue linked to suboptimal microwave pulse frequency for the object size [20]. This effect was more noticeable with the semi-circular than with the circular array.

B. Image Reconstruction Accuracy for Reduced Number of Transmission Channels in the Semi-Circular Array

In addition to the simulated results for Cases 1–4, we also reconstructed measured data from similar targets using the semi-circular array. Figs. 7 and 8 show the reconstructions for Case 1 with 56, 50, 36, and 14 transmission channels. Image accuracy remains stable as the number of channels is reduced, but when only 14 channels are used, clutter increases enough to potentially lead to the false conclusion of multiple reconstructed bleedings.

The impact of reducing the number of transmission channels was also analyzed using the same metrics as before. Localization errors were computed and plotted in Fig. 9 for both measured and simulated data. The measured data (Fig. 9(a) show greater variations in localization error, while the simulated data (Fig. 9(b) remain more stable. The results also indicate that cases with smaller blood phantoms, such as Case 3, are more challenging—here, localization stays stable down to 26 channels but then deteriorates as the target region shifts, and a successful reconstruction cannot be achieved at 14 channels. Case 4 is especially affected due to its deeper target and increased clutter, consistent with findings reported in [3].

Furthermore, the HWR results in Fig. 10(a) and Fig. 10(b) indicate that the reconstructed shape stays fairly consistent as the number of transmission channels decreases, with only minor variations. These variations can be attributed to a narrowing of the FWHM region, as seen in Fig. 7 and Fig. 8.

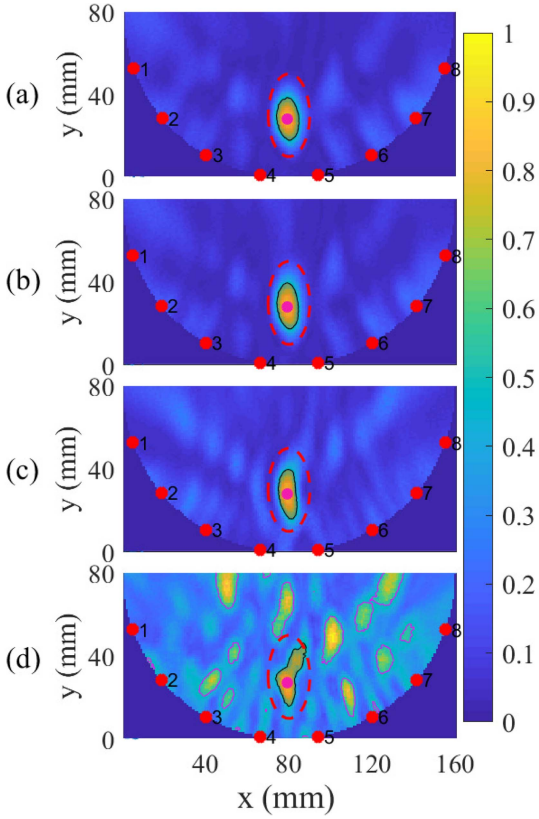

Fig. 7. Reconstructed images of measured Case 1 using (a) 56 channels (b) 50 channels (c) 36 channels (d) 14 channels.

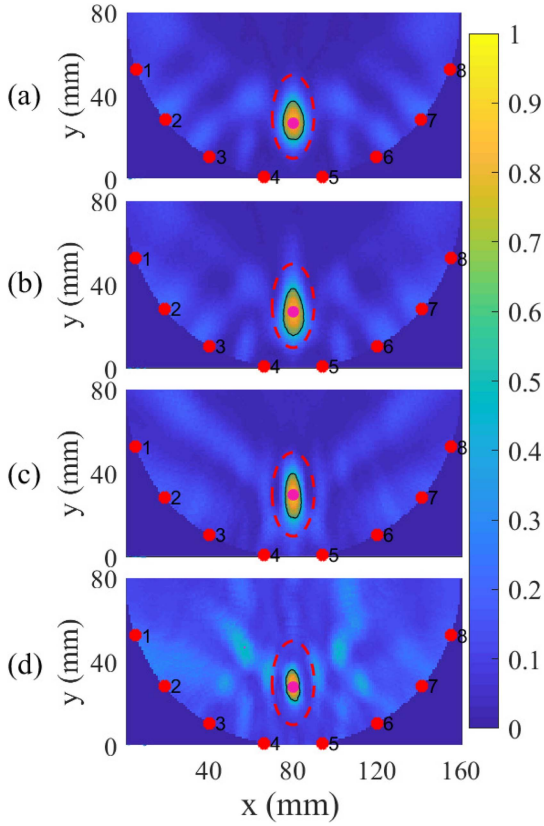

Fig. 8. Reconstructed images of simulated Case 1 using (a) 56 channels (b) 50 channels (c) 36 channels (d) 14 channels.

We calculated SCR and CNR for the four measured and simulated cases as a function of transmission channels, shown in Fig. 11. Both metrics remain fairly constant down to 44 channels, with occasional increases. Below 44 channels, SCR gradually decreases while CNR stays stable. This aligns with the visual results in Fig. 7 and Fig. 8, where object-background contrast (SCR) remains steady down to 36 channels, and clutter magnitude (CNR) remains unchanged.

Table I summarizes the metrics Δr, HWR, SCR, and CNR for different numbers of transmission channels. The parameters stabilize at around 36 channels and in most cases, increasing the number of channels beyond 44 provides no noticeable improvement. This trend is evident both quantitatively in the computed metrics and qualitatively in the corresponding reconstructed images (Figs. 7 and 8), which show negligible visual enhancement beyond this point.

IV. Discussions

Omitting a moderate number of transmission channels from distant antennas to reduce measurement time doesn't significantly affect the accuracy of the image reconstructions.

The objects were reconstructed within the expected bounds using both semi-circular and circular arrays. The circular array showed slightly better clutter rejection, especially in simulations

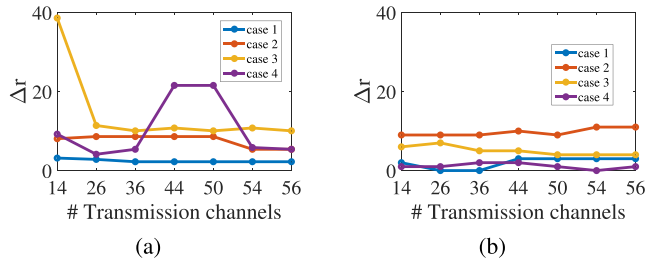

Fig. 9. Δr for (a) measurements and (b) simulations as a function of the number of channels.

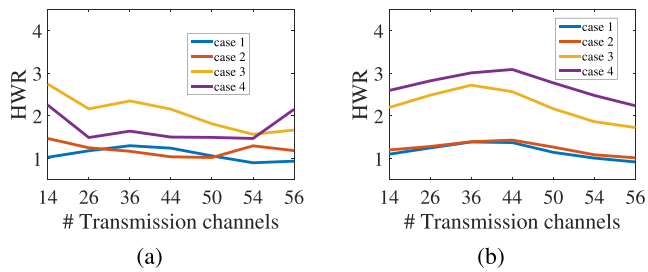

Fig. 10. HWR ratio as a function of the number of channels for (a) measurements and (b) simulations.

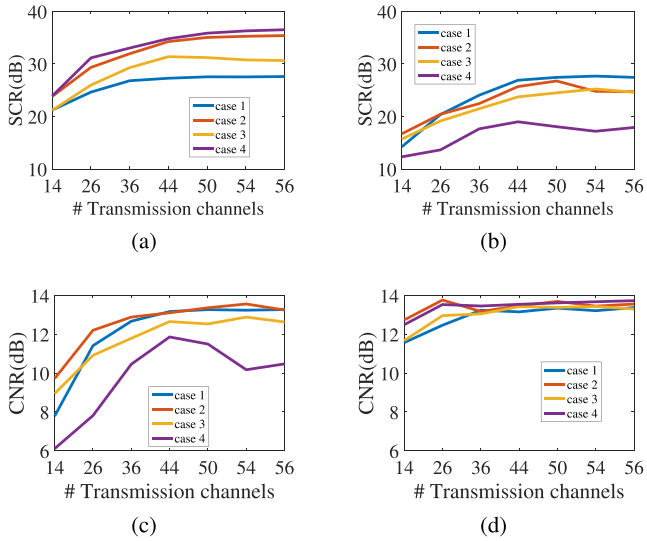

Fig. 11. SCR for (a) measurements and (b) simulations; and CNR for (c) measurements and (d) simulations.

TABLE I
Δr, HWR, SCR AND CNR FOR MEASUREMENTS (MEAS) AND SIMULATIONS (SIM) AS A FUNCTION OF THE NUMBER OF CHANNELS

# Tx ch.	$Case1$		$Case2$		$Case3$		$Case4$	
	Meas	Sim	Meas	Sim	Meas	Sim	Meas	Sim
	Δr							
56	2.24	3.0	5.39	11.0	10.0	4.0	5.39	1.0
54	2.24	3.0	5.39	11.0	10.8	4.0	5.83	0.0
50	2.24	3.0	8.60	9.0	10.0	4.0	21.5	1.0
44	2.24	3.0	8.60	10.0	10.8	5.0	21.5	2.0
36	2.24	0.0	8.60	9.0	10.0	5.0	5.39	2.0
26	2.83	0.0	8.60	9.0	11.4	7.0	4.12	1.0
14	3.16	2.0	8.06	9.0	38.6	6.0	9.22	1.0
	HWR							
56	1.03	1.1	1.47	1.2	2.75	2.2	2.25	2.59
54	1.18	1.25	1.25	1.28	2.16	2.49	1.49	2.82
50	1.30	1.39	1.17	1.39	2.35	2.72	1.64	3.01
44	1.24	1.37	1.04	1.43	2.16	2.57	1.50	3.09
36	1.06	1.15	1.02	1.27	1.81	2.17	1.50	2.77
26	0.901	1.01	1.30	1.09	1.57	1.86	1.47	2.48
14	0.939	0.92	1.19	1.02	1.67	1.73	2.15	2.24
	SCR							
56	27.4	27.6	24.7	35.4	24.6	30.6	17.9	36.5
54	27.7	27.5	24.8	35.3	25.2	30.8	17.2	36.3
50	27.4	27.6	26.8	35.0	24.5	31.2	18.1	35.9
44	26.9	27.3	25.7	34.3	23.7	31.4	19.0	34.8
36	24.1	26.8	22.5	32.0	21.5	29.3	17.7	33.0
26	20.4	24.6	20.4	29.3	19.2	26.0	13.7	31.2
14	14.2	21.2	16.7	23.8	15.7	21.2	12.3	23.9
	CNR							
56	13.3	13.4	13.3	13.6	12.6	13.3	10.5	13.7
54	13.2	13.2	13.6	13.5	12.9	13.4	10.2	13.7
50	13.3	13.3	13.4	13.7	12.5	13.4	11.5	13.6
44	13.2	13.2	13.1	13.5	12.7	13.4	11.9	13.5
36	12.7	13.2	12.9	13.2	11.8	13.1	10.5	13.5
26	11.4	12.5	12.2	13.8	10.9	13.0	7.81	13.5
14	7.79	11.6	9.72	12.7	8.94	11.7	6.11	12.5

involving bleedings near the skin or surface of the phantom, which aligns well with findings in [9]. Higher SCR were observed when blood phantoms were placed near the surface rather than deeper. This is because signals attenuate more and create more clutter when propagating deeper.

Our results indicate that reducing the number of transmission channels is feasible, particularly when prioritizing those with shorter antenna distances, as supported by [14], [15]. However, performance degrades below 36 channels (as seen in Table I), partly due to SCR limitations influenced by system dynamic range (DR) and signal-to-noise ratio (SNR). The exception was a smaller, deeper blood phantom, where increased signal attenuation and clutter led to significant reconstruction changes. This would also be a challenging scenario in the leg since deeper bleedings would be closer to the bone.

Our setup is limited to 8 antennas on the half-circle or 16 for a full-circle due to physical constraints. Theoretical analyses, with the degrees of freedom approach [21], indicate that $N = 26$ antennas would be required to fully sample the field in our application. $N \geq 2\beta_b a + 1$, where β_b is the real part of the background wave number and a is the radius of the imaging domain [22]. However, this theoretical estimate is based on far-field conditions, which do not apply to our near-field setup. Moreover, practical limitations such as the DR and SNR of the measurement system restrict the ability to fully exploit all available degrees of freedom [8], [23]. As shown in these studies, increasing the number of antennas beyond a certain point does not necessarily improve imaging performance if the system's DR is limited [8]. In fact, smaller arrays can offer increased robustness to measurement noise and modeling errors while still achieving acceptable image quality, particularly when the target is a small, localized variation, as in our application [23].

While this study uses a VNA for measurements, the system is designed with future SDR-based implementation in mind. Despite SDRs having lower dynamic range, the antenna configuration accounts for such limitations, so the core conclusions are expected to hold.

The goal is not exact field reconstruction but rather to just maintain acceptable accuracy. Using fewer antennas than the theoretical optimum can be compensated by additional signal processing techniques [11], [24].

The position of the reconstructed bleeding depends on the size of the blood phantom as well as on the position of the antennas but is still reconstructed within the boundaries of the blood phantom.

Fig. 11 shows a 10 dB difference in SCR between measurements and simulations, caused by simulation data being noise free and measured data containing noise [2], [25]. Moreover, simple phantoms were used, which somewhat limits the generalisability of the results. A more tissue like phantom and a more rigorous phantom study would for example include also bone. However the results show that the application is feasible and one could consider moving directly to clinical measurements in a future study.

The results show that the object's shape is more influenced by the antenna placement than the number of channels used, and viewing the target from multiple directions improves boundary information, though further research is needed. The evaluation metrics are inadequate for evaluating reconstructions of larger blood phantoms where the object splits into distinct regions, so these cases were evaluated qualitatively.

The size of the bleeding can vary significantly depending on factors such as local blood flow and muscle activation at the time of injury [26], [27]. However, the typical region of interest is generally a few centimeters in size. Our experimental setup and imaging resolution are designed to match this scale, and the results demonstrate adequate sensitivity for detecting such localized variations.

Our current bleeding models primarily resemble acute intramuscular bleedings [26], but other bleeding types, such as diffuse intramuscular or intermuscular bleedings, may present different imaging challenges and should be explored in future studies to improve clinical relevance.

V. Conclusion

This article is a step in the development of a microwave muscle rupture detector and deals with the aspects of minimizing measurement time, which improves usability and reduces the risk of motion artefacts. We investigated the minimum number of transmission channels needed to accurately reconstruct an image. Our results show that it is feasible to decrease the number of transmission channels from 56 down to 36 channels while limiting the reduction in SCR to less than 12%. The SCR serves as the limiting factor in further reduction; it remains stable initially but declines rapidly when fewer than 36 transmission channels are used. While reducing the number of transmission channels, we observed that the position of the reconstructed blood phantom remains consistent, although its shape becomes distorted. Given that our current goal is the detection of bleeding indicative of muscle rupture, we can accept the trade-off of reduced shape accuracy.

References

[1] S. K. Chu and M. E. Rho, "Hamstring injuries in the athlete," *Curr. Sports Med. Reports*, vol. 15, no. 3, pp. 184–190, May/Jun. 2016.

[2] L. Guerrero Orozco, L. Peterson, and A. Fhager, "Microwave antenna system for muscle rupture imaging with a lossy gel to reduce multipath interference," *Sensors*, vol. 22, no. 11, Apr. 2022, Art. no. 4121.

[3] L. G. Orozco, L. Peterson, and A. Fhager, "Muscle rupture microwave imaging with a lossy gel to reduce multipath interference," in *17th Eur. Conf. Antennas Propag.*, May 2023, pp. 1–5.

[4] X. Zeng and L. G. Orozco, "Measurement quality of a software defined radio system for medical diagnostics," *J. Eng.*, vol. 2022, no. 12, pp. 1162–1172, Sep. 2022.

[5] M. O'Halloran, D. Byrne, M. A. Elahi, R. Cruz Conceição, E. Jones, and M. Glavin, *Confocal Microwave Imaging*. Cham, Switzerland: Springer, 2016, pp. 48–49.

[6] T. Henriksson et al., "Clinical trials of a multistatic UWB radar for breast imaging," in *Proc. Loughborough Antennas Propag. Conf.*, Dec. 2011, pp. 1–4.

[7] H. M. E. Misilmani, T. Naous, S. K. A. Khatib, and K. Y. Kabalan, "A survey on antenna designs for breast cancer detection using microwave imaging," *IEEE Access*, vol. 8, pp. 102570–102594, 2020.

[8] R. Scapaticci, J. Tobon, G. Bellizzi, F. Vipiana, and L. Crocco, "Design and numerical characterization of a low-complexity microwave device for brain stroke monitoring," *IEEE Trans. Antennas Propag.*, vol. 66, no. 12, pp. 7328–7338, Dec. 2018.

[9] M. Klemm, J. A. Leendertz, D. Gibbins, I. J. Craddock, A. Preece, and R. Benjamin, "Microwave radar-based differential breast cancer imaging: Imaging in homogeneous breast phantoms and low contrast scenarios," *IEEE Trans. Antennas Propag.*, vol. 58, no. 7, pp. 2337–2344, Jul. 2010.

[10] M. O'Halloran, E. Jones, and M. Glavin, "Quasi-multistatic mist beamforming for the early detection of breast cancer," *IEEE Trans. Biomed. Eng.*, vol. 57, no. 4, pp. 830–840, Apr. 2010.

[11] X. Zhang, N. Du, J. Wang, A. Massa, and X. Ye, "Improving the imaging performance of microwave imaging systems by exploiting virtual antennas," *IEEE Trans. Microw. Theory Techn.*, vol. 72, no. 10, pp. 5734–5744, Oct. 2024.

[12] B. Maklad, C. Curtis, E. C. Fear, and G. G. Messier, "Neighborhood-based algorithm to facilitate the reduction of skin reflections in radar-based microwave imaging," *Prog. Electromagnetics Res. B*, vol. 39, pp. 115–139, 2012.

[13] M. A. Elahi, M. Glavin, E. Jones, and M. O'Halloran, "Artifact removal algorithms for microwave imaging of the breast," *Prog. Electromagnetics Res.*, vol. 141, pp. 185–200, 2013.

[14] S. A. Shah Karam, D. O'Loughlin, B. L. Oliveira, M. O'Halloran, and B. M. Asl, "Weighted delay-and-sum beamformer for breast cancer detection using microwave imaging," *Measurement*, vol. 177, Jun. 2021, Art. no. 109283.

[15] A. Vayyeti and A. K. Thittai, "Euclidian-weighted non-linear beamformer for conventional focused beam ultrasound imaging systems," in *Proc. 43rd Annu. Int. Conf. IEEE Eng. Med. Biol. Soc.*, Dec. 2021, pp. 3684–3687.

[16] B. M. Asl and A. Mahloojifar, "Minimum variance beamforming combined with adaptive coherence weighting applied to medical ultrasound imaging," *IEEE Trans. Ultrason., Ferroelectr., Freq. Control*, vol. 56, no. 9, pp. 1923–1931, Sep. 2009.

[17] H. Been Lim, N. Thi Tuyet Nhung, E. -P. Li, and N. Duc Thang, "Confocal microwave imaging for breast cancer detection: Delay-multiply-and-sum image reconstruction algorithm," *IEEE Trans. Biomed. Eng.*, vol. 55, no. 6, pp. 1697–1704, Jun. 2008.

[18] M. Klemm, I. J. Craddock, J. A. Leendertz, A. Preece, and R. Benjamin, "Radar-based breast cancer detection using a hemispherical antenna array—Experimental results," *IEEE Trans. Antennas Propag.*, vol. 57, no. 6, pp. 1692–1704, Jun. 2009.

[19] E. Porter and D. O'Loughlin, "Pathway to demonstrating clinical efficacy of microwave breast imaging: Qualitative and quantitative performance assessment," *IEEE J. Electromagn., RF, Microw. Med. Biol.*, vol. 6, no. 4, pp. 439–448, Dec. 2022.

[20] A. Fhager, P. Hashemzadeh, and M. Persson, "Reconstruction quality and spectral content of an electromagnetic time-domain inversion algorithm," *IEEE Trans. Biomed. Eng.*, vol. 53, no. 8, pp. 1594–1604, Aug. 2006.

[21] O. Bucci and G. Franceschetti, "On the degrees of freedom of scattered fields," *IEEE Trans. Antennas Propag.*, vol. 37, no. 7, pp. 918–926, Jul. 1989.

[22] I. Catapano et al., "On quantitative microwave tomography of female breast," *Prog. Electromagnetics Res. B*, vol. 97, pp. 75–93, Oct. 2009.

[23] O. M. Bucci, L. Crocco, R. Scapaticci, and G. Bellizzi, "On the design of phased arrays for medical applications," *Proc. IEEE Proc. IRE*, vol. 104, no. 3, pp. 633–648, Mar. 2016.

[24] A. Zamani, A. M. Abbosh, and A. T. Mobashsher, "Fast frequency-based multistatic microwave imaging algorithm with application to brain injury detection," *IEEE Trans. Microw. Theory Techn.*, vol. 64, no. 2, pp. 653–662, Feb. 2016.

[25] P. M. Meaney, "Addressing multipath signal corruption in microwave tomography and the influence on system design and algorithm development," *Open Access J. Biomed. Eng. Biosciences*, vol. 1, no. 1, Feb. 2018, Art. no. 102.

[26] L. Peterson and P. Renstrom, *Sports Injuries: Prevention, Treatment and Rehabilitation*. Boca Raton, FL, USA: CRC Press, Taylor & Francis Group, 2017.

[27] M. Conforti, "The treatment of muscle hematomas," in *Muscle Injuries in Sport Medicine*, G. N. Bisciotti and C. Eirale, Eds. Rijeka, Croatia: IntechOpen, 2013, ch. 7, pp. 204–205. doi 10.5772/56903.

Laura Guerrero Orozco received the M.Sc. degree in biomedical engineering from the Chalmers University of Technology, Gothenburg, Sweden, where she is currently working toward the Ph.D. degree in electrical engineering. Her current research interests include electromagnetic imaging and biomedical applications of microwaves.

Lars Peterson received the M.D. and the Ph.D. degrees in fracture of the neck of the talus from Gothenburg University, Gothenburg, Sweden, in 1966 and 1974, respectively. He was a Specialist of general surgery and Specialist of orthopaedic surgery with Sahlgrenska University Hospital, Gothenburg, in 1972 and 1973, respectively. He was appointed as an Associate Professor in 1980 and Professor of orthopedic surgery in 2000. He was the President from 2001 to 2002. He was the Head Physician with the Swedish National Team for Ice Hockey and Soccer. He is currently a Professor emeritus of orthopaedic surgery with Gothenburg University. He pioneered the treatment of articular cartilage injuries using autologous chondrocyte transplantation first cell therapy in orthopaedics. He has authored or coauthored more than 200 articles, reviews, and book chapters. For 38 years, Lars Peterson has been a member of the Sports Medical Committee of FIFA and Founding Member of F-MARC (FIFA Medical Assessment and Research Center). In addition, he was one of the Founders of ICRS (International Cartilage Regeneration and Joint Repair Society). In 2007, the first European elected member of "The Hall of Fame" of the American Orthopaedic Society of Sports Medicine. He was the recipient of 2010 "The Duke of Edinburgh Prize" for "Outstanding contribution to international education in Sports Medicine".

Andreas Fhager (Member, IEEE) received the M.Sc. degree in engineering physics, and the Ph.D. degree in electrical engineering from the Chalmers University of Technology, Gothenburg, Sweden, in 2001 and 2006, respectively. He was appointed Docent of electrical engineering with the Chalmers University of Technology, in 2011. His current research interests include electromagnetic imaging methods for breast cancer detection, stroke and trauma diagnostics, and other biomedical applications of microwaves.